Journal of Low Temperature Physics (2020) 199:737–744
https://doi.org/10.1007/s10909-020-02351-3

Progress in the Development of Frequency-Domain Multiplexing for the X-ray Integral Field Unit on Board the Athena Mission

H. Akamatsu[1] · L. Gottardi[1] · J. van der Kuur[2] · C. P. de Vries[1] · M. P. Bruijn[1] · J. A. Chervenak[3] · M. Kiviranta[4] · A. J. van den Linden[1] · B. D. Jackson[1,2] · A. Miniussi[3] · K. Ravensberg[1] · K. Sakai[3] · S. J. Smith[3] · N. Wakeham[3]

Received: 20 August 2019 / Accepted: 14 January 2020 / Published online: 28 January 2020

Abstract
Frequency-domain multiplexing (FDM) is the baseline readout system for the X-ray Integral Field Unit on board the Athena mission. Under the FDM scheme, TESs are coupled to a passive LC filter and biased with alternating current (AC bias) at MHz frequencies. Using high-quality-factor LC filters and room-temperature electronics developed at SRON and low-noise two-stage SQUID amplifiers provided by VTT, we have recently demonstrated good performance with the FDM readout of Mo/Au TES calorimeters with Au/Bi absorbers. We have achieved a performance requested for the demonstration model with the single-pixel AC bias ($\Delta E = 1.8$ eV) and nine-pixel multiplexing ($\Delta E = 2.6$ eV) modes. We have also demonstrated 14-pixel multiplexing with an average energy resolution of 3.3 eV, which is limited by nonfundamental issues related to FDM readout in our laboratory setup.

Keywords Transition-edge sensors · X-ray calorimeters · X-ray astronomy · Athena · X-IFU

1 Introduction

Athena is a second L-class mission in the ESA's cosmic vision program [1]. To answer questions like *How does the ordinary matter assemble into the large-scale structures that we see today?* and *How do black holes grow and influence the*

✉ H. Akamatsu
h.akamatsu@sron.nl

[1] SRON Netherlands Institute for Space Research, Utrecht, The Netherlands

[2] SRON Groningen Netherlands Institute for Space Research, Groningen, The Netherlands

[3] NASA GSFC, Greenbelt Road, Greenbelt, MD 20771, USA

[4] VTT, Espoo, Finland

Universe?, Athena employs two main focal plane instruments: X-ray Integral Field Unit (X-IFU [2]) and Wide Field Imager (WFI [3]). The X-IFU instrument consists of an array of ∼ 3000 transition-edge sensor X-ray microcalorimeters (TES calorimeter) with a high spectral resolution $\Delta E = 2.5\,\mathrm{eV}$ up to 7 keV ($E/\Delta E \sim 2800$). Due to strictly limited available electrical and cooling power in space, the multiplexing technology is one of the key technologies for X-IFU.

We are developing the frequency-domain multiplexing (FDM) readout of TES calorimeters for the X-IFU instrument. Under the FDM scheme, each TES is connected with a passive LC filter and biased with alternating current (AC bias) at MHz frequencies. Each resonator should be separated beyond their detector response to avoid cross talk between neighboring resonators. To satisfy the requirement of the X-IFU, a multiplexing factor of 40 pixels/channel in a frequency range from 1 to 5 MHz is required. Therefore, frequency separation for the X-IFU will be 100 kHz.

2 NASA/GSFC TES Calorimeter Array and Experimental Setup

2.1 TES X-ray Microcalorimeter Array

In this paper, we report spectral resolution and multiplexing results of TES calorimeter arrays from NASA/GSFC group. The TES is made of Mo/Au bilayer with a BiAu-mushroom-type absorber. The basic information about TES arrays is summarized in Table 1. Detailed characterization of these devices under AC bias is presented in [4].

2.2 Experimental Setup

For details of the experimental setup, the readers are recommended to refer to previous works [5, 6]. For the completeness, we are using a cryogen-free dilution unit [7], which has a cooling power of 400 μW at 110 mK. A germanium thermistor (Lake Shore GR50) is implemented in the Cu experimental plate, which has a temperature sensitivity $\alpha\,(\equiv \frac{T}{R}\frac{\mathrm{d}R}{\mathrm{d}T}) \sim 5$. At 60 mK, the base temperature in this report, the typical temperature stability is about 0.5–0.7 $\mu\mathrm{K}_{\mathrm{rms}}$ over a day [6].

SRON in-house lithographical LC filters are operated at the same temperature of the detector. These LC resonators show high Q factors as large as 10,000 [8]. The inductance was designed to be 2 μH. By tuning capacitance values, 18 resonators span 1–5 MHz. 0.75 Ω bias shunt resistance and 1:25 capacitive voltage divider

Table 1 Basic information of NAS/GSFC TES calorimeter and our electrical circuits

	TES size ($\mu\mathrm{m}^2$)	R_{N} (mΩ)	T_{c} (mK)	Critical inductance @ 20 % of Rn (nH)	Transformer ratio	Effective inductance (nH)
Device A6	100×100	35–35	89	550	1:3.0	274
Device A7	120×120	30–40	87	670	1:2.0	565

are implemented in the detector stage. To match SQUID dynamic range and tune damping inductance [9], we are using a superconducting transformer with a primary inductance of 48 nH. The typical coupling coefficient is about 0.92–0.94. The transformation ratio for each detector is also given in Table 1. Room-temperature high-μ metal and superconducting Nb are employed for the magnetic shielding. Superconducting Helmholtz coils are implemented in the experimental plate to cancel the remnant magnetic field and investigate magnetic field dependence, respectively. For the spectral performance evaluation, ^{55}Fe source is mounted on the Nb shield. The count rate is tuned to be $\sim$ 1 cps. For the FDM readout, SQUID is one of the most important components. We are using two-stage VTT SQUIDs amp consisting of six-array front end and 184×4 array amplification SQUIDs. The mechanical vibrations are damped by Kevlar wires [10]. To increase the bandwidth of the FDM, we compensate for the delay between the room temperature and 50 mK by using Baseband feedback (BBFB) [11]. The SQUID signal is demodulated and remodulated with phase shift by an FPGA board before it is fed back. We are using SRON in-house analog (SQUID controller and LNA) and digital (demodulation, BBFB, etc) electronics. Data were obtained in 40 M samples/s, decimated to 156 k samples/s and demodulated around the resonant frequency of each LC filter.

3 Results

3.1 Performance Under Single-Pixel Mode and Multiplexing Experiments

To investigate potential limitations, we first start characterizations of the detector performance under AC bias. For this measurement, we used Device A6 (100 μm^2 TES). The bias points were set around $R/R_{\mathrm{N}} \sim 0.2$. The remnant magnetic field was canceled by the Helmholtz coils. The long-term temperature drift correction was performed by using TES baseline current and pulse height information. Using the zero energy (0 keV), Mn-K$_\alpha$ (5.9 keV) and Mn-K$_\beta$ (6.5 keV) information, the energy nonlinearity was also corrected. The typical energy nonlinearity factor is about 1–2 %. The energy spectra were fitted with the Mn-K$_\alpha$ line model by minimizing the total C-stat value [12] to avoid undesired fitting bias.

The best performances under AC bias at 1.25 and 4.40 MHz are $\Delta E = 1.8 \pm 0.2$ eV and 2.1 ± 0.2 eV, respectively (Fig. 1) although typical range of the performance is $\Delta E \sim 2.0 - 2.5$ eV. At the low bias frequency, for the first time, we have achieved DC bias compatible performance under AC bias [13, 14]. At higher frequency, there is a slight degradation, which can be the impact of AC loss [15], AC Josephson effect [16] and contributions from the room-temperature electronics. Both performances are better than predictions from the integrated noise equivalent power (NEP). Because of the large inductance, the pulse excursion is getting larger. This leads to the noise decrease during the pulse. Therefore, better X-ray resolutions than NEP resolution will be achieved. Therefore, in this paper, we will mainly focus on X-ray performances.

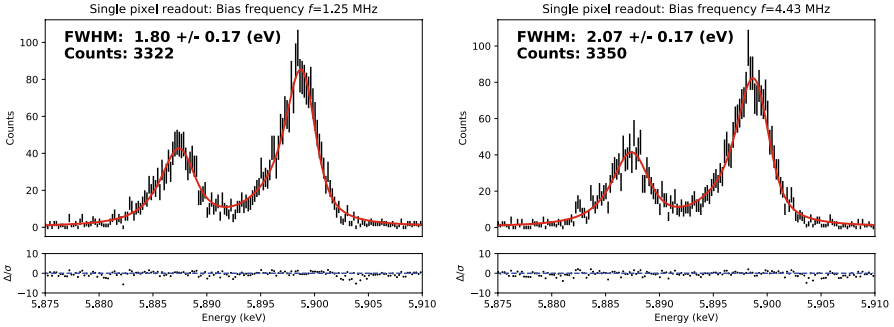

Fig. 1 Energy spectrum of Mn Kα complex from ^{55}Fe source. Black bar and red solid line indicate measured spectrum and the best-fit model, respectively. Bottom panel shows the normalized residual in the unit of (data model)/statistical error. Left and right panels show spectrum at AC bias frequency of 1.25 MHz and 4.43 MHz in the single-pixel readout mode, respectively (color figure online)

We perform multiplexing experiments with two different conditions: (1) Device A6 and nine-pixel MUX with 200 kHz separation and (2) Device A7 and 14-pixel MUX with 100 kHz separation. The results are shown in Fig. 2. The summed spectral resolutions are $\Delta E = 2.6$ eV, 3.3 eV for nine-pixel MUX and 14-pixel MUX, respectively. In the 200 kHz MUX case, the summed spectral resolution surpasses

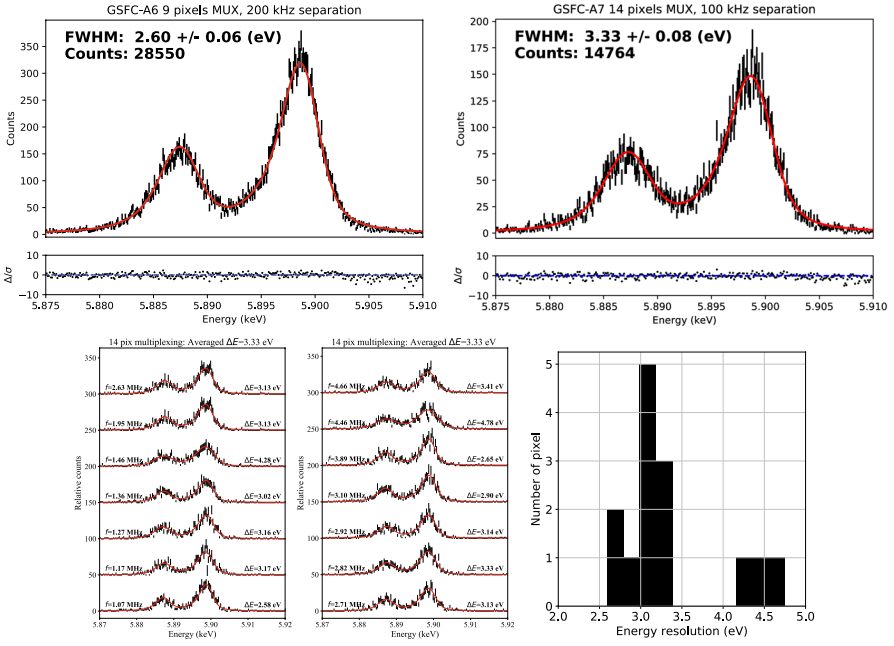

Fig. 2 (Top) Summed spectra of nine-pixel MUX with 200 kHz (Device A6) and 14-pixel MUX with 100 kHz (Device A7), respectively. (Bottom left) 14 individual spectra in the 14-pixel MUX mode. (Bottom right) Histogram of the energy resolution in 0.2 eV bin (color figure online)

the requirement of the demonstration model of X-IFU instrument ($\Delta E < 3$ eV) although the frequency separation did not match the X-IFU requirement (100 kHz separation). Therefore, we took an approach to further increase multiplexing number rather than improving the spectral performance to identify potential bottlenecks with 100 kHz separation and given configurations. In the 100 kHz separation case, the resonator frequencies span across 1.0–4.7 MHz. The summed energy resolution ($\Delta E \sim 3.3$ eV) degrades considerably from 200 kHz separation configuration ($\Delta E \sim 2.6$ eV). The bottom right panel in Fig. 2 shows a histogram of energy resolutions. There are roughly three populations: (1) around 2.6 eV, (2) around 3.0 eV and (3) 4.4–4.6 eV. We figured out that these populations can be explained by (1) impacts of intermodulation line noises and (2) influences from neighboring bias voltages.

3.2 Impact of the Intermodulation Line Noise

Any nonlinearities will generate spurious line noises via the intermodulation mechanisms. Such nonlinearity can be caused by the SQUID amplifiers, the DACs and even the passive components on board. For the worse-performance pixels ($\Delta E \sim 4.5$ eV), we confirmed the presence of line noises within the thermal band.

For the DAC case, the effect of the nonlinearity can be removed by using carriers in a frequency arrangement where the frequency spacing between all subsequent carriers is the same and where each carrier frequency is an integer number times that spacing. In this way, all distortion products will fall on a carrier and no spurious line noises will be present between the carriers.

To confirm the impact of the line noises, we performed an additional three-pixel MUX experiment with 100 kHz separation configuration. The resonant frequencies are $f = 1.07$ MHz (Ch0), 1.17 MHz (Ch1) and 1.27 MHz (Ch2). In the single-pixel mode, all three pixels show good performances around 2.2–2.5 eV (Table 2). Under three-pixel MUX mode (Fig. 3 top left), although the other two pixels show moderate changes, the central pixel (Ch1: $f = 1.17$ MHz) shows significant degradation from $\Delta E = 2.20$ eV to 5.58 eV. As expected, there is a significant line noise component in the Ch1 noise spectrum (Fig. 3 bottom left). The line noise is located at the frequency at which the detector is still sensitive (orange shaded area), meaning the detector feels modulation at line noise frequency in their bias voltage.

The impact of this intermodulation line noise can be avoided by changing bias frequency. However, due to the high-Q LC filter, changing bias frequency generates

Table 2 Detector performances @ 6 keV under three-pixel MUX mode (unit of eV)

	Single-pixel mode	Three-pixel MUX without FSA	Three-pixel MUX with FSA
Ch0 ($f = 1.07$ MHz)	2.52 ± 0.18	2.78 ± 0.18	2.93 ± 0.14
Ch1 ($f = 1.17$ MHz)	2.20 ± 0.15	5.58 ± 0.18	3.07 ± 0.16
Ch2 ($f = 1.27$ MHz)	2.39 ± 0.18	2.85 ± 0.17	3.01 ± 0.16

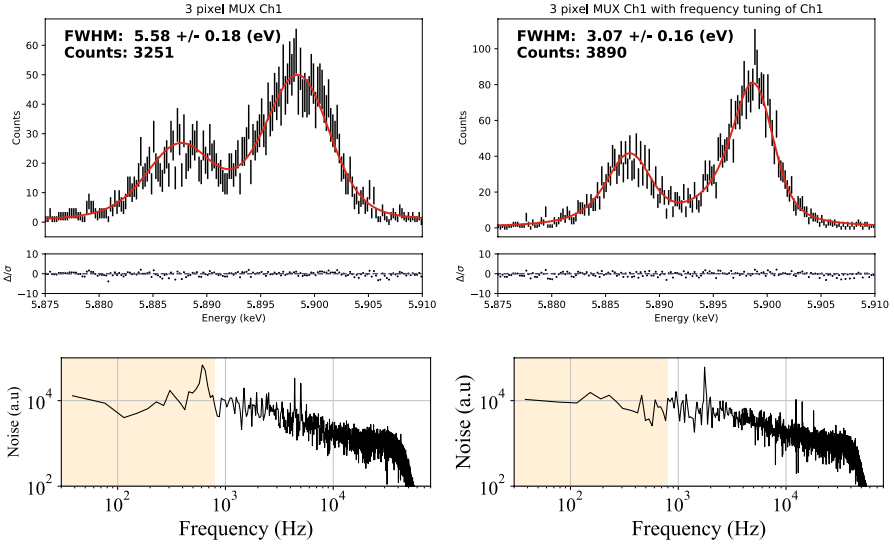

Fig. 3 (Top) Under 3 pixel MUX mode, spectra of Ch1 ($f = 1.17$ MHz) without (left) and with FSA (right). (Bottom) Noise spectra of Ch1 without (left) and with FSA (right). The orange shaded area indicates two times the detector's thermal band (color figure online)

a different electrical circuit. As shown in the left panel of Fig. 4 (gray points), the detector performance has a strong bias frequency dependency. To mitigate this dependency, we are developing the frequency shift algorithm (FSA). The details of FSA are given in the previous works [17]. Under the FSA scheme, the on-resonance

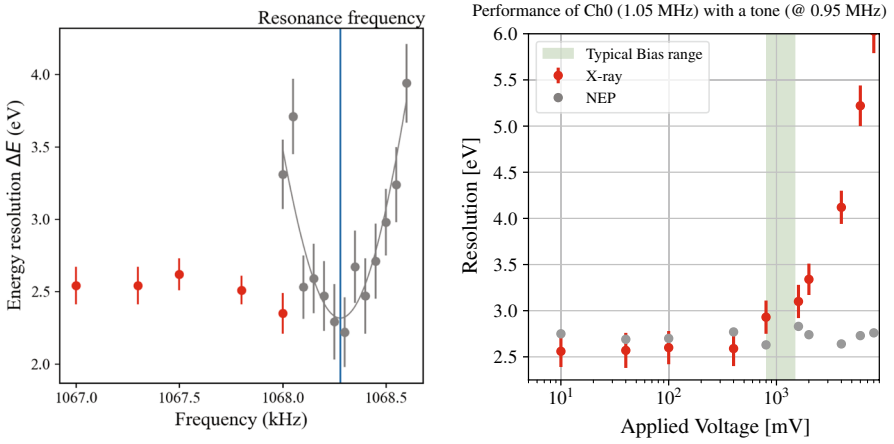

Fig. 4 (Left) Single-pixel X-ray performance with (red) and without (gray) FSA. The resonant frequency is indicated by the blue vertical line. (Right) Single-pixel X-ray performance with additional AC bias tone at 100 kHz lower frequency. Gray and red points indicate integrated NEP and X-ray resolution, respectively. Green shaded region indicate typical bias voltage for $R \sim 0.2Rn$ (color figure online)

detector performance and response will be kept with different bias frequencies. The red points in Fig. 4 show the performance with FSA with different bias frequencies. Although the detector performance across wide frequency range will be available with FSA, it still needs fine-tuning to obtain the same performance at the resonance frequency.

Back to the three-pixel MUX experiment, we applied FSA to Ch1 with 400 Hz shift to kick the intermodulation line noise out from the detector thermal band. As shown in the right top panel in Fig. 3, FSA improves the performance significantly from 5.6 to 3.1 eV without any influence on the other two pixels within given statistical errors (Table 2). Noise spectrum after frequency shift shows a clear difference in terms of the location of the line noise, which shifted toward a higher frequency regime.

3.3 Influences from Neighboring AC Bias Voltages

As demonstrated in Sect. 3.2, the three-pixel MUX experiment also shows around 3 eV performance after removing the impact of the intermodulation line noise. It is consistent with the highest peak in the bottom right panel of Fig. 2. We figured out that the degradation to ~ 3 eV could be the interferences from neighboring AC bias voltages. The effect was already reported in our earlier works [18]. If the detector electrical bandwidth ($\sim R/L$) is too large, the detector is still sensitive to neighboring AC bias voltage, resulting the modulations in TES current with Δf (resonant frequency–neighboring bias frequency) interval. In this case, the integrated NEP resolution will not be affected. but X-ray resolution will be degraded by the modulations.

To confirm this effect, we perform an experiment: single-pixel X-ray measurement with additional tone at 100 kHz separated frequency and different bias voltages. The right panel in Fig. 4 shows the results. As expected, the NEP resolutions are constant across different bias voltages. On the other hand, X-ray resolutions show a strong dependence on the applied voltages. When the applied voltage is small, there is no effect on the performance. However, once the voltage is getting close to the typical TES voltages (green shaded area), the performances degrade significantly. This means TES has still too large electrical bandwidth to be independent from neighboring bias voltages. This means that TES has still dependence on the neighboring voltages because of too large electrical bandwidth.

This effect can be solved in three ways: (1) by using a larger frequency separation, (2) by applying a phase window [18] and (3) by using a narrower electrical bandwidth detector. From X-IFU instrument point of view, options 1 and 2 will not be the final solution. Therefore, option 3 will be the solution. The electrical bandwidth can be suppressed by making TES critically damped. However, as shown in Table 1, TESs are working close to critical damping at 14-pixel MUX experiment. To narrow down the electrical bandwidth, we need different devices, which have much slower detector response time, allowing us to use larger inductance. Here, we note that detector designs of GSFC-A6 and A7 are a factor 2–3 faster than X-IFU requirements. Currently, new devices which will satisfy the X-IFU requirements and further larger setups are under development. Once they are ready, we are expecting

that FDM demonstration will have another jump in terms of the number of multiplexed pixels.

4 Summary

We are developing a Frequency-domain multiplexing technology for the X-IFU on board the Athena mission. By using the state-of-art TESs, cryogenic and room-temperature electronics, we confirmed that the TES performance under AC bias is compatible with DC bias case ($\Delta E \sim 1.8$ eV). We also demonstrated 9-pixel (200 kHz) and 14-pixel (100 kHz) MUX readouts with 2.6 and 3.3 eV summed performances, respectively. The observed degradation from 200 kHz to 100 kHz frequency separation can be explained by (1) impact of the intermodulation line noise (Sect. 3.2) and (2) influences from neighboring AC bias voltage (Sect. 3.3). Future X-IFU device, which will be a factor 2–3 slower than the current one, will improve the situation in both intermodulation line noises and interference from neighboring bias voltage.

Acknowledgements The authors would like to thank Martijn Schoemans, Dick Boersma, Marcel van Litsenburg, Patrick van Winden and Bert-Joost van Leeuwen for their precious/continuous help. The authors also thank an anonymous referee for constructive comments. SRON is supported financially by NWO, the Netherlands Organization for Scientific Research.

References

1. D. Barret, A. Decourchelle, A. Fabian et al., arXiv e-prints. (2019). arXiv:1912.04615
2. D. Barret, T. Lam Trong, J.-W. den Herder et al., SPIE, 106991G (2018)
3. A. Rau, N. Meidinger, K. Nandra et al., arXiv e-prints. (2013). arXiv:1308.6785
4. L. Gottardi et al., These proceedings
5. H. Akamatsu, L. Gottardi, J. Adams et al., J. Low Temp. Phys. **176**, 591 (2014)
6. H. Akamatsu, L. Gottardi, C.P. de Vries et al., J. Low Temp. Phys. **184**, 436 (2016)
7. https://leiden-cryogenics.com/
8. M.P. Bruijn, A.J. van der Linden, L. Ferrari et al., J. Low Temp. Phys. **193**, 661 (2018)
9. J. van der Kuur, L.G. Gottardi, H. Akamatsu et al., SPIE 99055R (2016)
10. L. Gottardi, H. van Weers, J. Dercksen et al., Rev. Sci. Instrum. **90**, 055107 (2019)
11. R. den Hartog, D. Boersma, M. Bruijn et al., in *American Institute of Physics Conference Series*, vol. 261 (2009)
12. J.S. Kaastra, A&A **605**, A51 (2017)
13. S.J. Smith, J.S. Adams, S.R. Bandler et al., SPIE 99052H (2016)
14. A.R. Miniussi, J.S. Adams, S.R. Bandler et al., J. Low Temp. Phys. **193**, 337 (2018)
15. K. Sakai, J.S. Adams, S.R. Bandler et al., J. Low Temp. Phys. **193**, 356 (2018)
16. L. Gottardi, S.J. Smith, A. Kozorezov et al., J. Low Temp. Phys. **193**, 209 (2018)
17. J. van der Kuur, L. Gottardi, H. Akamatsu et al., J. Low Temp. Phys. **193**, 626 (2018)
18. J. van der Kuur, P.A.J. de Korte, H.F.C. Hoevers et al., IEEE Trans. Appl. Supercond. **13**, 638 (2003)